

Surfactant-Free Facile Synthesis of Nickel Oxalate Monodispersed Particles in Novel Morphologies with Fine Tuning of the Experimental Variables

Khalida Akhtar*, Ghazala Irum and Muhammad Gul

*National Centre of Excellence in Physical Chemistry, University of Peshawar,
Peshawar-25120, Khyber Pakhtunkhwa, Pakistan*

khalida_akhtar@yahoo.com*

(Received on 12th November 2021, accepted in revised form 2nd March 2022)

Summary: The surfactant or shape modifier used in the synthesis of monodispersed uniform fine particles affected the performance of the prepared powder in its applications. The present investigation is related to synthesizing colloidal uniform fine particles of nickel oxalate in novel morphologies under an optimized set of reaction conditions without using any surfactant or shape modifier. SEM results revealed that the reactant concentration significantly affected the characteristics of the precipitated solids, which ranged from gel to dispersion of discrete particles. Particles of uniform morphological features were obtained under an optimized set of experimental conditions, i.e., reactant concentration, temperature, aging time, etc. The molar ratio of the precursors affected the particle's growth mechanism as the spherical morphology of the particles changed to a cubic shape by increasing nickel ion concentration in the recipe at 25 °C. The cubic morphology transformed into toffee shape bigger particles of a 0.5 axial ratio by increasing the reaction medium's thermal energy. The synthesized particles were characterized by various physical techniques, which confirmed the product as the monodispersed pure NiC₂O₄·2H₂O particles.

Keywords: Nickel oxalate; Fine particles; Controlled precipitation.

Introduction

Nanostructured materials present the most challenging area of current scientific and technological research on behalf of the unusual phenomena related to their unique shape, size, and structure [1, 2, 3]. Tuning of the particle morphology and size can enhance the electronic, magnetic, optical, and photocatalytic properties of functional material [4]. It has been reported that the photocatalytic efficiency for the degradation of dye depended on the nature and morphological features of the particles of the nanocatalysts [5, 6]. It is worth mentioning that material properties are primarily dependent on the reaction conditions and the synthesis route followed [7]. Therefore, investigations on a facile and economical route for morphology-controlled synthesis are needed to empower nanomaterial novel intrinsic properties in many fields of technological importance [8, 9]. Nickel oxalate nanostructures are particularly appreciated for various applications such as energy storage [10-12], electrochemical glucose sensing [13], antiferromagnetic material [14], catalyst [15], and a precursor for nickel oxide nanoparticles [10-16].

Many methods have been used to synthesize nickel compounds on nanoscale [4, 11, 17-21]. However, liquid precipitation has the edge over other methods due to its simplicity, control of particle size and morphology, and cost-effectiveness [22]. In this regard, the oxalate precursor route is advantageous

due to the low reaction temperature and homogeneity of the particles [1]. The latter has been reported to prepare oxalate/oxide nanostructures of various metals like copper [23], iron [24], cobalt [25] and zinc [9, 26]. Particles of nickel oxalate have been prepared by researchers in various morphologies, such as plates [27], nanowires [20], nanofibres [18, 28], nanospheres [29, 30], nanocubes, and nanorods [30]. However, many of these studies included either surfactants or various additives to control particle morphology and size, where the particle size distribution was significantly high. The scarcity of the literature on the systematic exploration of the role of various experimental parameters to govern the morphology and size of the nickel oxalate particles was a motivation for the current work.

Therefore, the present study is aimed to investigate the effect of synthetic conditions like the concentration of the precursor reactants, reaction temperature, aging time, and mixing protocols to establish a rational design for producing monodispersed nickel oxalate particles of novel morphologies.

Experimental

Materials

Chemically pure oxalic acid and nickel chloride [Merck] were used as received. Based on the

*To whom all correspondence should be addressed.

requirements of the stoichiometric ratio, solutions of nickel chloride and oxalic acid were prepared in Pyrex glassware using distilled water. Before use, all the solutions were filtered through a 0.2µm size membrane to remove impurities. Stock solutions were used within a week in the current work.

Synthesis of monodispersed particle systems

Particles were synthesized from oxalic acid and nickel chloride mixed in various ratios (i.e., $[\text{Ni}^{2+}]/[\text{C}_2\text{O}_4^{2-}] = 0.25, 0.66, 1.5$ and 4.0), in a temperature range of $25\text{-}80\text{ }^\circ\text{C}$ for various aging times ($5\text{-}40$ min). The suspension was filtered through vacuum filtration, washed, and stored in tight packings for further characterization.

Characterization

The particle morphology of the synthesized material was investigated by SEM (JSM-5910, JEOL). The prepared powder material was layered with a thin gold coating by a fine coater (JFC-1600, JEOL). For the structural investigation and crystallinity, selected batches of the particles were tested with an XRD (JEOL JDX-3532) with Cu K_α radiations of wavelength 0.154 nm . In each test, the material was scanned from $10^\circ - 80^\circ$ of the 2θ at a step angle of 0.05° and scan rate at $0.1^\circ/\text{sec}$. The crystalline nature of the test material was identified from the obtained XRD data with the help of JDX-3500 software.

A thermal study was performed using TGA/DTA (Diamond Perkin Elmer analyzer). For this analysis, the specific quantity of the test material was heated in an air atmosphere to $600\text{ }^\circ\text{C}$ at $10\text{ }^\circ\text{C}/\text{min}$ in the crucible using electromagnetic balance. Similarly, the functional groups on the surface of the synthesized material were investigated by recording the FT-IR spectra in the $4000\text{-}400\text{ cm}^{-1}$ range using Shimadzu, IR Prestige-21. The test sample during analysis was held by the diffuse reflectance accessory (DRS-8000A).

Results and Discussion

By aging the aqueous mixtures, containing the nickel chloride and oxalic acid in appropriate ratio at room temperature, light green powder of nickel oxalate was produced according to the following reaction:



Effect of the reactant concentration on the particle's morphology

Oxalic acid and nickel chloride were mixed in various ratios and aged for $10\text{-}40$ minutes at room temperature. The synthesized powder of all the experiments was assessed for its morphology using SEM. In most synthesis trials, the polydispersed particle systems of irregular morphological features were precipitated, as shown in Fig. 1. It was observed from the SEM analysis that particle morphology had strongly influenced by the given reaction conditions. The experiments determined that the parameters like the amount of reactants, the reaction time, and the temperature of the formed particles in the reaction mixture were the main features to regulate the particle shape and size. By tailoring the reactant concentration in the medium, the as-synthesized spherical particle transformed to cubic morphology under constant aging and reaction temperature. From these observations, the applied reaction conditions were optimized in a regular way to establish a recipe for the synthesis of nickel oxalate monodispersed particles. The used approach worked and uniform particles of nickel oxalate dihydrate were prepared under controlled reaction conditions. Fig. 2 depicts images of the formed particles precipitated under the captioned technological parameters. The SEM images displayed particles with spherical and cubic shapes prepared under various reaction conditions, as listed in the description of the corresponding Fig.

From the observed results, it can be stated that the nuclei grew into cubic shape at a low concentration of nickel salt. On the other hand, spherical particles of nickel oxalate resulted when the precursor salt concentration was significantly high. The growth in the spherical shape of the particles showed the nondirectional aggregation method of the primary formed particles under the applied experimental conditions. Besides, the particle's morphology was found sensitive to the temperature of the reaction medium. The cubic shape morphology was obtained at room temperature, while the particles of toffee shape were formed when the temperature was increased to $50\text{ }^\circ\text{C}$. It is worth mentioning that the synthesized cubic and spherical morphologies of nickel oxalate particles, in the captioned adjusted parameters, were a fresh addition to material science. To the best of our information, no such experimental methodology in the absence of surfactants has been reported until now.

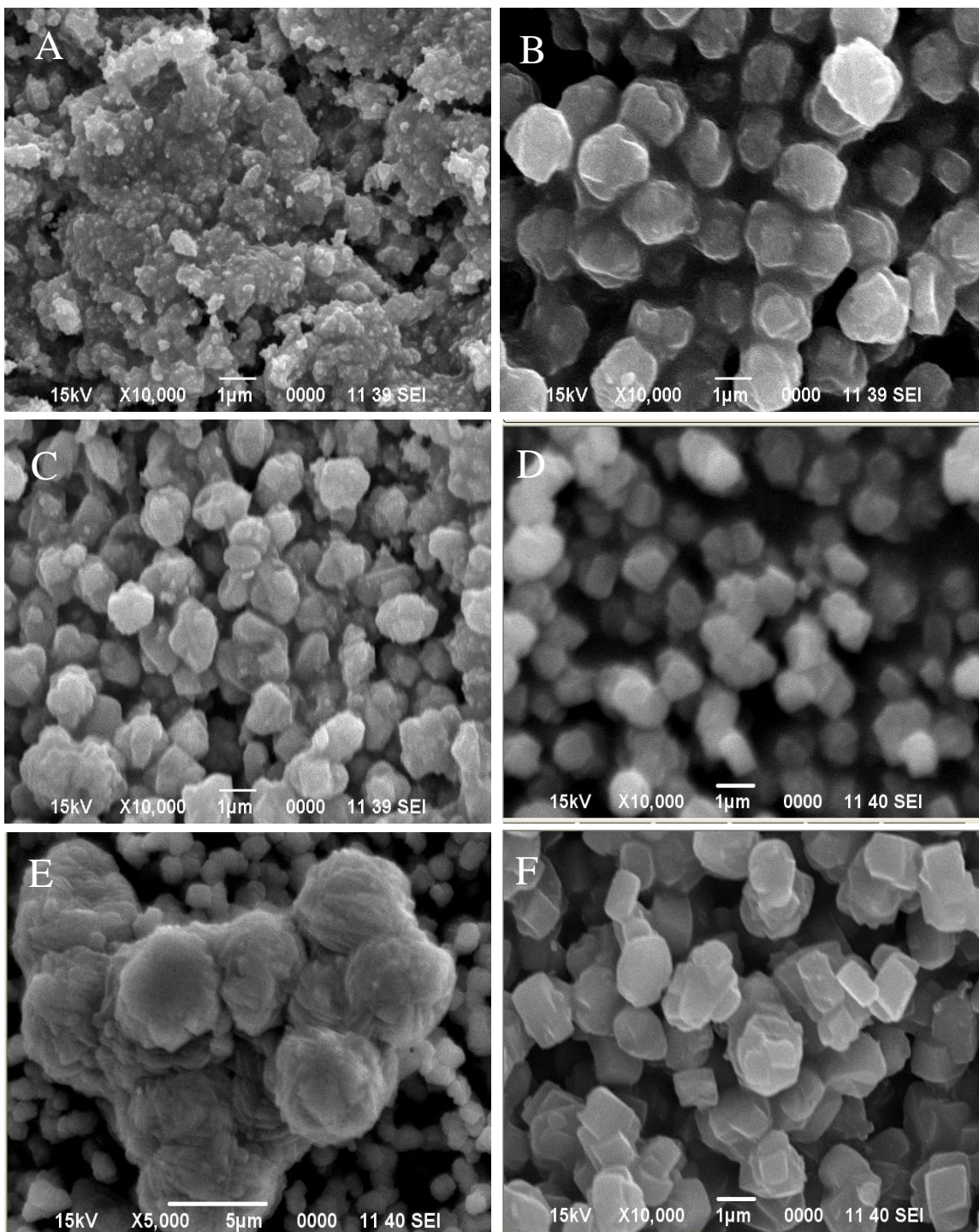


Fig. 1: Scanning electron micrographs (SEM) of the trials of nickel oxalate particles synthesized by precipitation method using nickel chloride and oxalic acid as a precipitating agent under different experimental conditions.

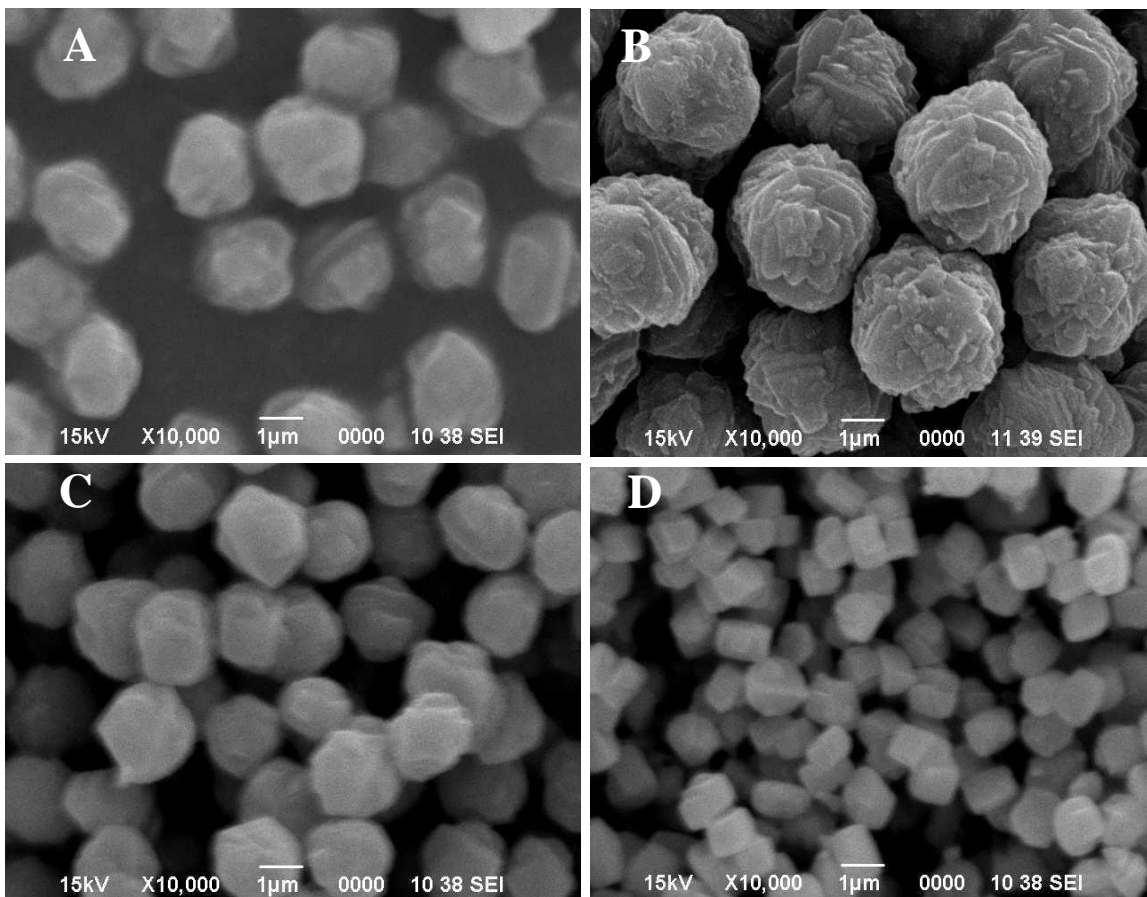


Fig. 2: SEM micrographs of the particle systems of different morphologies produced at the $[\text{Ni}^{+2}]/[\text{C}_2\text{O}_4^{-2}]$ molar ratio equal to (A) 0.25, (B) 0.66, (C) 1.5, and (D) 4, at 25 °C.

Under the constant reaction conditions of pH, mixing protocol, and temperature, a regular change in the precursor's molar ratio was found to have a noticeable effect on the nickel oxalate particle morphology. The shape of the synthesized spherical particles systematically changed to cube shape as a function of the reactant's ratio (nickel salt/ oxalic acid) when mixed at room temperature at the initial pH of 6.8, as shown in Fig. 2. Nevertheless, the Ni^{2+} reacts with oxalate ions ($\text{C}_2\text{O}_4^{2-}$) at a stoichiometric ratio (1:1) to form nickel oxalate; the final product's particle shape was noted to be dependent on Ni^{2+} to $\text{C}_2\text{O}_4^{2-}$ ratio. Therefore, it was motivating to explore the practical strategy of the product chemistry. The observed outcomes explained that the Ni^{2+} to $\text{C}_2\text{O}_4^{2-}$ ratio significantly affected the morphology of the precipitated particle. In this study, diverse ratios of Ni^{2+} and $\text{C}_2\text{O}_4^{2-}$ have been studied. At metal ion to oxalate of 0.25, the nuclei matured into tiny rectangular sheets that were the source for the end particles. It is thought that second stage nucleation started afterward and the secondary formed particles

arranged on the surfaces of the rectangles, as shown in Fig. 2A.

When the reactant ratio was changed (0.66), the conditions were favorable for the particles to grow and acquired spherical morphology with a rough surface. Careful examination of the particle surface (SEM; Fig. 2B) showed that the particles were not formed from the growth process of nuclei. Instead, the small particles formed an aggregate of spherical shape for obtaining stability while decreasing the surface energy. In this case, the primary rectangular sheets were also surrounded by secondary particles. Still, due to the equivalent amount of precursors nickel and oxalate ions in the reaction mixture, the high second stage nucleation covered the surfaces of rectangular sheets (SEM; Fig. 2B). In a further experiment, the ratio was increased (1.5), which gave the same results. However, the concentration of oxalate ions was low compared to the nickel ions; therefore, the number of the secondary formed nuclei was not sufficient to fully shield the faces of formed rectangular particles (Fig.

2C). The following molar ratio of (nickel)/oxalate) = 4 displayed an impressive effect by changing the shape of particles from spherical shape to cubic. Here, the applied concentration of oxalate ions was such that it prohibited the initiation of the second nucleation. Therefore, the primary formed particles grew in both faces and attained cubic morphology (Fig. 2D). These results confirmed that the nickel to oxalate ions ratio is one of the important technical parameters for regulating the desired morphology of as-synthesized particles.

The familiar classical crystallographic theory describes two processes for synthesizing material, i.e., nucleation step and crystal growth. A low concentration of nickel salt initiated a low degree of saturation in the medium, which resulted in a slow rate of nucleation. In this situation, superficial and epitaxial crystal growth predominates, favoring perfect crystallinity. In contrast, a high cation concentration initiated many nucleations, therefore, losing control of the crystal's growth [31]. The data obtained are presented in Fig. 3.

Aging time effect on the particle's morphology

The aging time of the reaction under the same optimized experimental conditions was investigated for the as-prepared particle systems. For this system, the synthesis recipes of the spherical and cubic shape (SEM, Figs. 2A and D) were tried under the constant technological conditions only with the change in aging time (15-40 min) to trap the particle growth track. SEM images of the particle system

synthesized under different time intervals are shown in Figs. 4 and 5.

Figs. 4A and B explored the morphology and showed that many small units were stacked together to form a single particle. It is supposed that the primary nuclei grew equally in three dimensions by the process of aggregation and ended up in 30 min with well-developed full-grown spherical particle morphology (Fig. 4C). The particle growth was disturbed after 30 min of aging, resulting in disrupted spherical particles (Fig. 4D).

During experiments, the medium was not turbid uniformly; instead, the turbidity progressed slowly down from the top and covered the entire mixture. Therefore, it is assumed that the multiple nucleations were continuous up to a specific time period and were dominated by the growth process. Due to Brownian motion, the primarily formed tiny nuclei were supposed to grow in a rectangular manner and instantaneously spread in the mixture. As the turbidity proceeded down, the fresh nuclei precisely organized themselves on the formed rectangular sheet faces, as presented in Fig 3. When the reaction mixture became completely turbid, and each of the quantity of the reactants was deficient in forming nuclei anymore, the only growth process started in the reaction medium (Fig. 4D). Small portions of the reaction mixture at specific time periods were collected to trap the growth extent at different time intervals and analyzed by SEM.

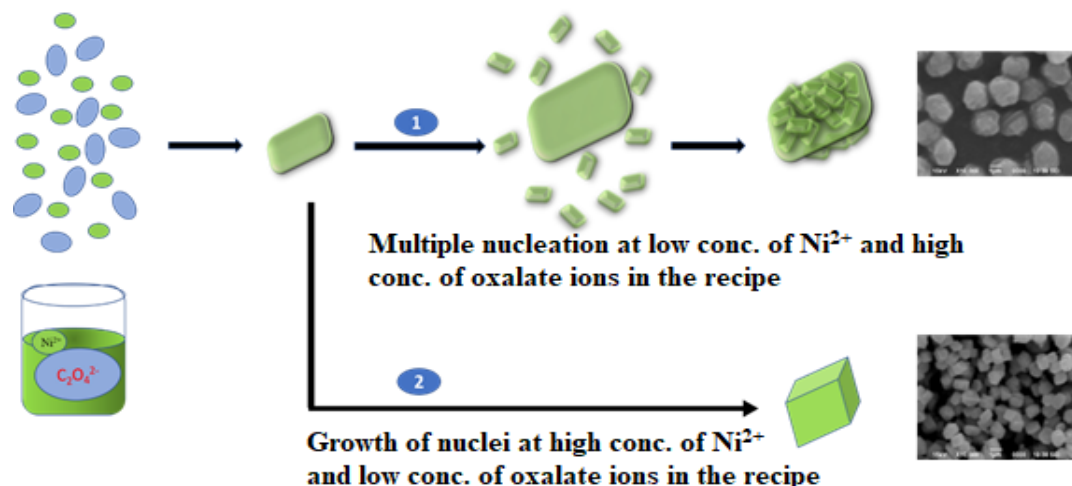


Fig. 3: Schematics of the mechanism of particle formation at (1) high concentration of nickel, and (2) low concentration of nickel in the reaction medium.

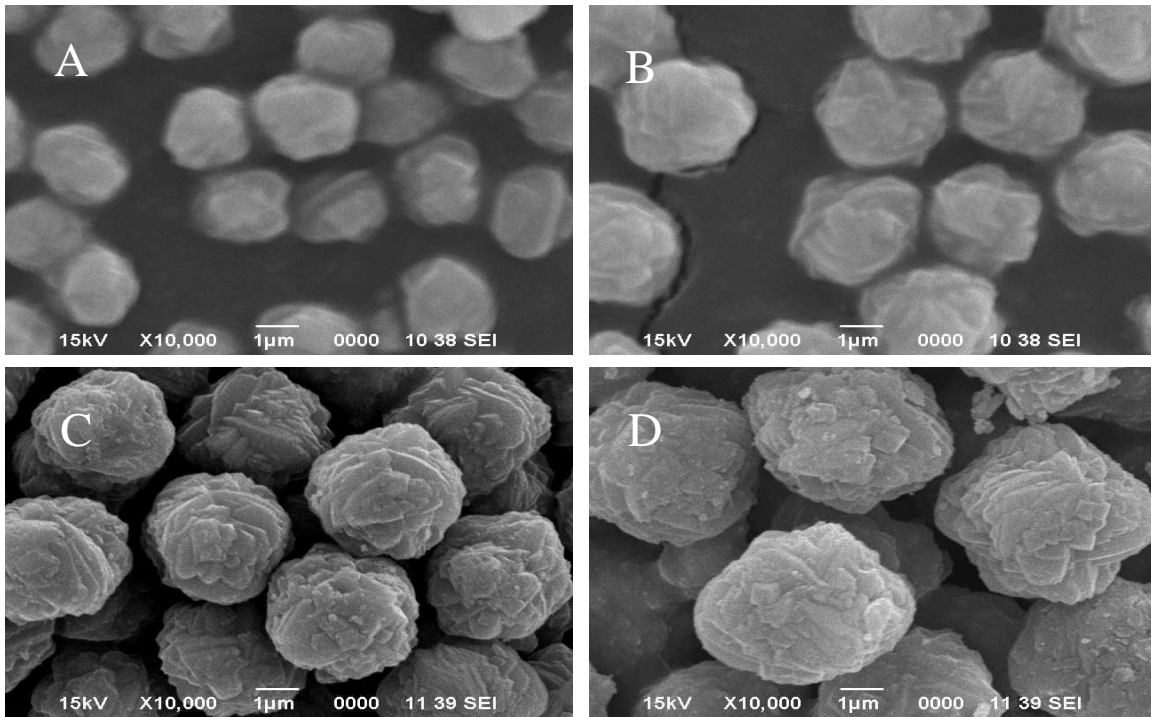


Fig. 4: SEM micrographs of the particles at the aging time of (A) 15 min, (B) 20 min, (C) 30 min and (D) 40 min; following the rest of experimental parameters like that of SEM, Fig. 2A.

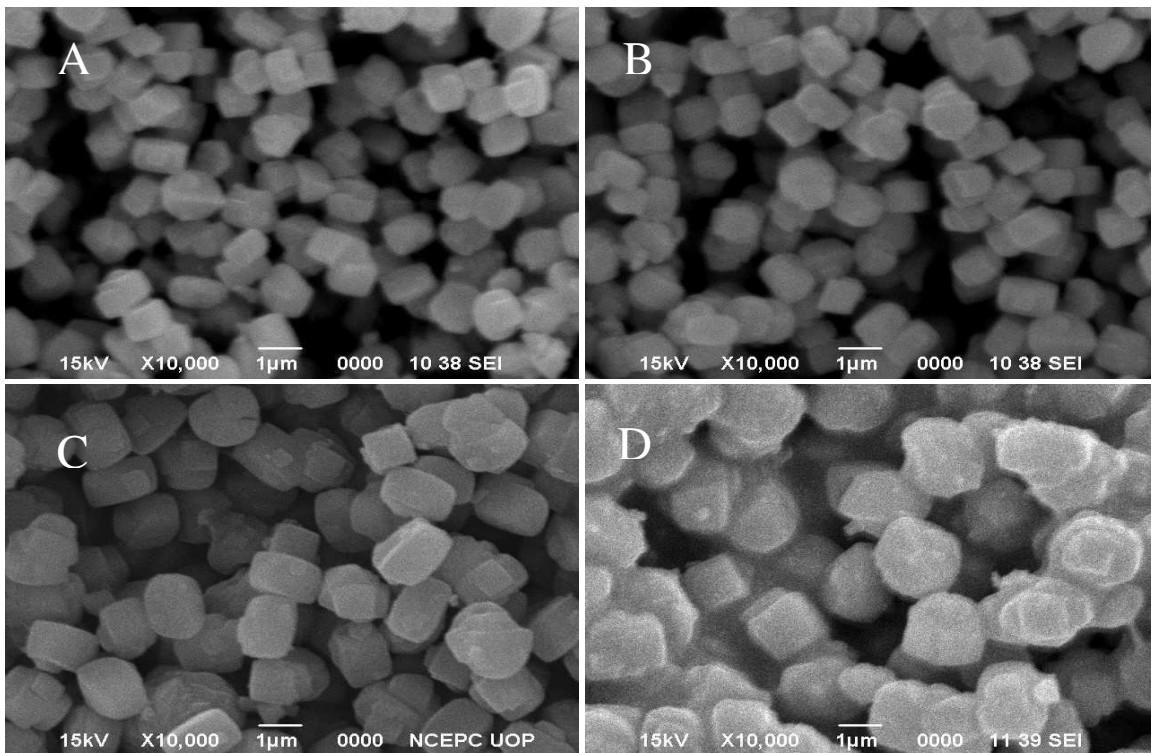


Fig. 5: SEM micrographs of the particles at the aging time of (A) 15 min, (B) 20 min, (C) 30 min and (D) 40 min; following the rest of experimental parameters like that of SEM, Fig. 2D.

Similarly, the cubes (Fig. 2D) increased in size with aging time up to 30 min (Fig 5A-C) and the further aging destroyed the particle morphology (Fig. 5D). The growth mechanism of the particle is formerly defined schematically in Fig. 3.

The SEM images showed that the size of the particle increased when the reaction time was increased while all other parameters were kept constant. It was observed (Fig. 4) that the average particle's diameter was increased from 2.2 μm to 4.2 μm with the increase in reaction time from 15 min to 40 min. In the case of cubes (Fig. 5), the average diameter grew to $\approx 1.5 \mu\text{m}$ with the increase in aging (15 to 40 min). It may be due to the surface growth of the formed nuclei because ions in the medium were deposited on the particles. Subsequently, the particles progressively grew in size due to supersaturation. It was detected that the aging of the reactant mixture has a significant effect on the uniformity and particle size distribution of the system [32]. It is to be stated that elongated particles of 1.5 (Fig. 5C) were observed at 30 min of aging, which acquired tetragonal geometry.

Nevertheless, particle morphology became disturbed with an increase in the aging time. The reaction parameters with aging time are depicted in the respective Fig captions (Figs. 4 and 5). It was observed the size of the spherical and cubic shape particles was almost linearly increased with the reaction aging (Fig. 6). Interestingly, the reaction conditions were optimized, which reproducibly formed particles with uniform morphological features.

Effect of the reaction temperature

The particles shown in Fig. 2D were further treated to evaluate the influence of temperature on the morphology of the synthesized particles. The experiments were performed by varying the reaction temperatures from 25-80 $^{\circ}\text{C}$ while other experimental parameters were constant. It is generally observed that the rate of reaction is affected by the reaction temperature, which disturbs the size and morphology of the particle of the precipitated material. A typical sample shown in Fig. 7 was obtained at the temperature of 25-80 $^{\circ}\text{C}$ from the reaction mixture of nickel chloride and oxalic acid ($[\text{Ni}^{2+}]/[\text{C}_2\text{O}_4^{2-}] = 4$) at 6.8 initial pH. The SEM images (Fig. 7) explored that monodispersed nickel oxalate particles in a uniform cubic shape with narrow size distribution were observed at 25 $^{\circ}\text{C}$ (Fig. 7A). According to the

well-known precipitation theory (LaMer's theory), single-stage nucleation is required to produce uniform particles.

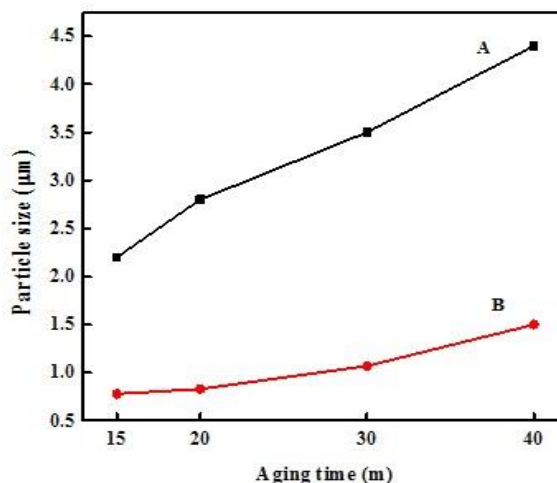


Fig. 6: Variation of the average particle's size of (A) spherical particles shown in Figs. 4 A-D and (B) cubic particles shown in Figs. 5A-D with aging time.

In contrast, multiple nucleations result in polydispersity of the particle system with the formation of secondary nuclei. The reaction medium temperature of 40 $^{\circ}\text{C}$ increased the particle size, which resulted in some sort of particle aggregation (Fig. 7B). Further increase in thermal energy (50 $^{\circ}\text{C}$ and above), the cubic shape particles (Fig. 7A) were transformed into toffee shape (Figs. 7C-F) with the addition of some small particles due to the propagation of secondary nucleation.

The accelerated particle growth with the increase in reaction temperature may be explained based on the viscosity and ionic mobility of the reaction mixture. An increase in synthesis temperature decreased the medium viscosity and increased the mobility of ions or diffusion, which eventually favored the rate of particle growth as the probabilities for particle encounters were more. Therefore, particle growth starts in three dimensions. Though, the path of increased growth is finally investigated by the orientation (preferred) of the formed crystal. It is supposed that the system's supersaturation changes inversely with the medium temperature.

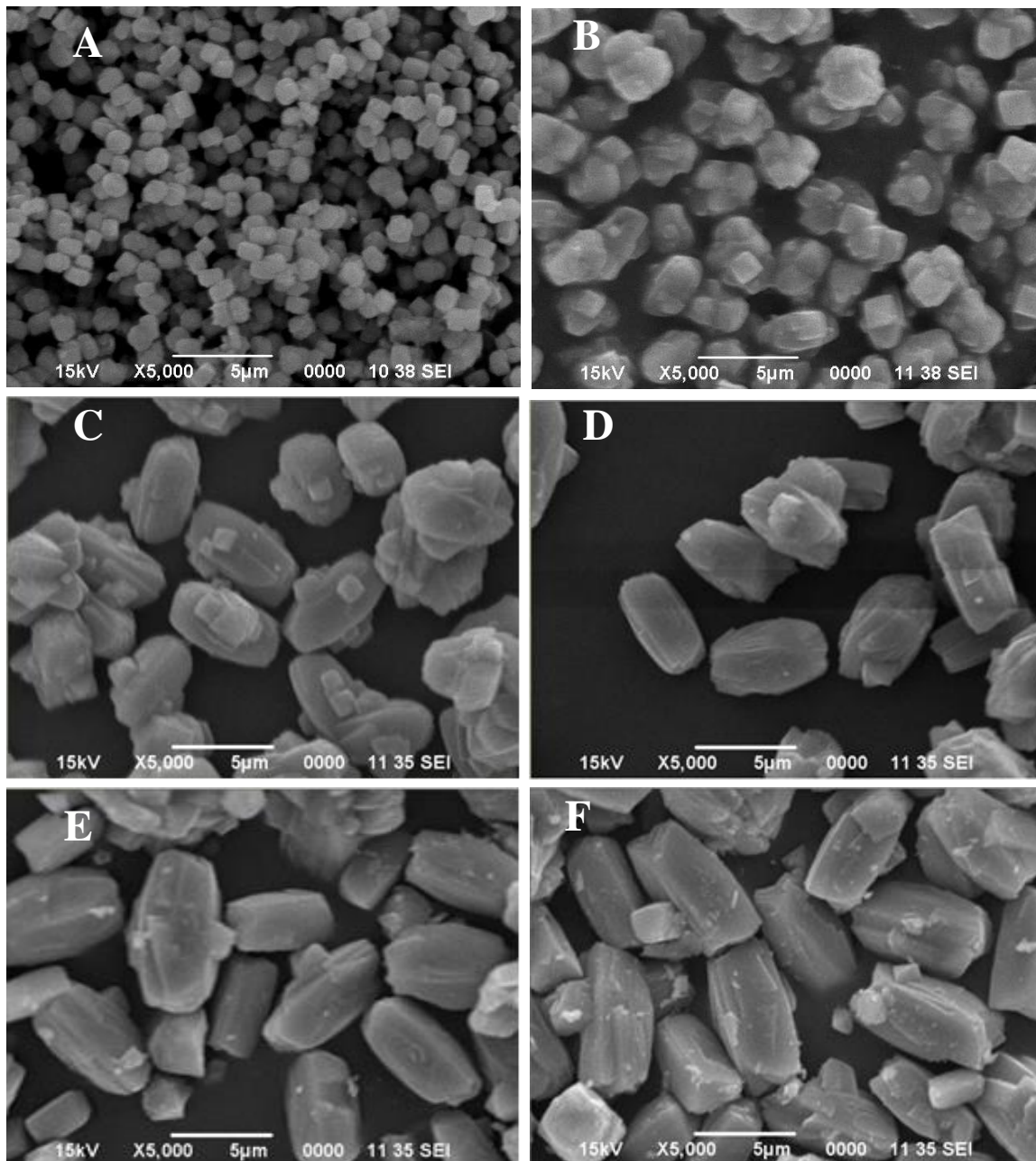


Fig. 7: SEM micrographs of the particles synthesized at the temperature (A) 25 °C, (B) 40 °C, (C) 50 °C, (D) 60 °C, (E) 70 °C, and (F) 80 °C, following the recipe of particles shown in SEM; Fig. 2D.

Consequently, the system favors relatively the particle growth more than the secondary nucleation. It is, therefore, considered necessary to perform the precipitation reaction at low reaction temperature for small size particles of nickel oxalate [33, 34]. The same behavior of particle increase with a rise in temperature from 10 to 80 °C was investigated elsewhere [35]. But, the reported particles were irregular in size at low temperatures, whereas, in this work, low temperatures favored the monodispersity. Graphical representation of

the axial ratio and increase in particle size is shown in Fig. 8. It depicted that the particles prepared at various temperatures (Figs. 7A and B) were nearly cubic with almost one axial ratio. However, the system precipitated at 40 °C (Fig 7B) has agglomerated large size particles compared to the particles shown in Fig. 7A. For high medium temperature (Fig. 7F), the particle's width and length slowly increased, achieving a constant axial ratio (~ 0.5), which displayed the particle's length of twofold to the width.

Table-1: List of the wavenumber positions (FT-IR; Fig. 9) at which the chemical groups on the solids absorb the IR radiations.

Band position (cm ⁻¹)	Chemical group	Vibration mode	Reference
3384	OH ⁻	Stretching vibration	[17, 33]
1650	OH ⁻ C=O	Bending vibration stretching mode	[17, 33]
1319	CO ₂ ⁻	stretching mode	[33, 34]
1359	C-O	stretching mode	[33, 34]
829	O-C=O	Bending	[34]
493	Ni-O	Stretching mode	[34]

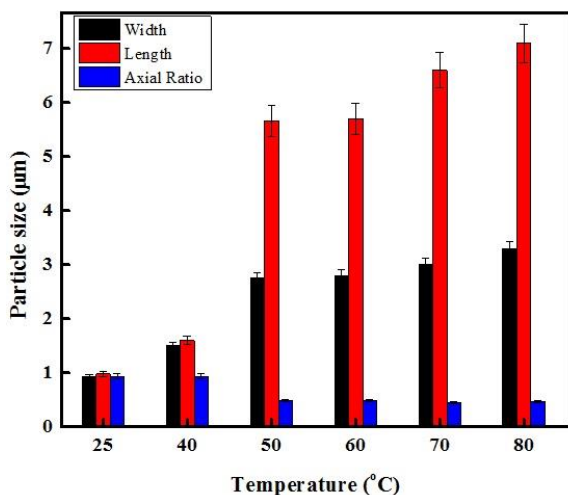


Fig. 8: Statistics of the effect of reaction temperature on the properties of particulate powder synthesized at (A) 25 °C, (B) 40 °C, (C) 50 °C, (D) 60 °C, (E) 70 °C, and (A) 80 °C, following the recipe of particle system shown in SEM; Fig. 2D.

The SEM images of the as-prepared particles shown in Fig. 7 indicated manifold nucleations at 40 °C. The newly synthesized moieties formed aggregates in the medium (Fig. 7B) for stability due to high surface energy as noted during precipitation experiments that the reaction mixture turbid from the top, which slowly proceeded downward. It showed continuous nucleations with the succeeding precipitated particles growth. In such experiments, optimization of the reaction conditions for synthesizing monodispersed particle systems was a tough job that was accomplished effectively at a low temperature. Though, at synthesis temperature > 30 °C, there is still more to explore about the governing reaction parameter for the synthesis of uniform fine particle systems.

FTIR spectroscopic analysis

The structural functionality was explained based on the characteristic positions of the IR bands in the FTIR spectra (Fig. 9) of nickel oxalate uniform

particle systems synthesized by reproducible recipes in different morphologies (SEM; Figs. 2A and B, Fig. 4C, and Fig. 5C). The band observed at 1645 cm⁻¹ and 3373 cm⁻¹ in FTIR profiles was due to the symmetrical stretching vibration of hydrogen bond of C₂O₄⁻² ions (Vas(OH) and Vas(OH)) [2, 22]. Similarly, the splitting of a prominent peak at ~1354–1312 cm⁻¹ was due to vibrations of oxalate (C₂O₄⁻²) (Vas(C-O), Vas(C-C) and δ(O-C=O)) carboxylate group [2, 36]. Furthermore, the small bands near ~490 and 830 cm⁻¹ were respectively assigned to the stretching of oxalate and Ni-O bond [37]. The relationship of these bands established that the analyzed particles were NiC₂O₄ (hydrated). It is worth mentioning that the precursor's molar ratio affected the particle's size and morphology; however, the spectra of the analyzed samples stayed unchanged, as depicted in Fig. 9. It exhibited that the material structure was independent of the precursors (nickel salt and oxalic acid solution) mixing as dihydrated nickel oxalate was precipitated in all experiments. The peaks observed in the FTIR spectra (Fig. 9) have been arranged in Table-1.

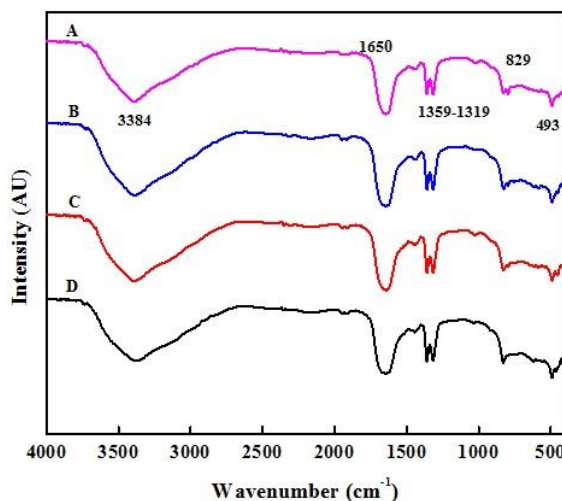


Fig. 9: FTIR spectra of as-prepared particles shown in (A) SEM; Fig. 2A, (B) SEM; Fig. 2B, (C) SEM; Fig. 4C, and (D) SEM; Fig. 5C.

XRD analysis

The phase purity and crystal structure of the selected particle systems (SEM; Figs. 2A and B, Fig. 4C, and Fig. 5C) were investigated by X-ray diffractometry (Fig. 10). The crystalline nature of the analyzed samples was confirmed from the observed XRD profiles, which were nearly identical for all samples. All the significant peaks noted in the XRD profiles (Fig. 10A-D) harmonized well with the standard diffraction data (PDF # 14-0742) [38], as matched through a well-known software (JDX-3500), which identified that the analyzed material was nanocrystalline NiC_2O_4 of orthorhombic structure. The strong diffraction peak of (202) shown in the XRD pattern (Figs. 10A-D) indicates nickel oxalate's preferential growth. Likewise, the locations of the peaks identified at 2θ values of 18.75° , 22.70° , 30.15° , and 35.55° respectively related to the (202), (004), (400), and (022) reflections from crystal planes. The absence of any additional peak in the detection limit of X-rays diffraction confirmed the pure and single-phase nickel oxalate dihydrate for the test material. Besides, the present results matched those described by Rakshit *et al.* [4] though their synthesis route for nickel oxalate was the dispersion method. These interpretations became supportive in exploring the fact that the synthesis method had a minor effect on its bulk features [39].

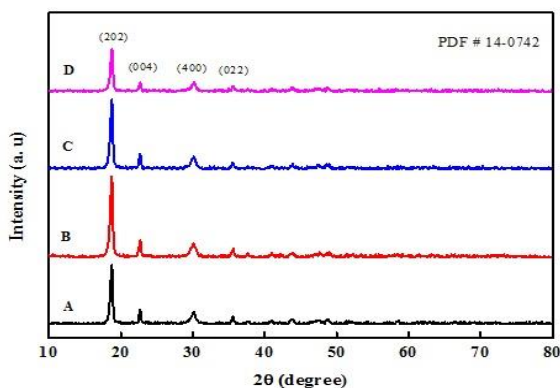


Fig. 10: XRD pattern of as prepared particles (A) SEM; Fig. 2A, (B) SEM; Fig. 2B, (C) SEM; Fig. 4C, and (D) SEM; Fig. 5C.

Moreover, the significant peaks data in the XRD profiles (Fig. 10) were used in the well-known Debye Scherrer's equation (Equation-2) [40] to calculate the average crystallite size of the as-synthesized nickel oxalate particles and the results are listed in Table-2.

$$D = 0.94\lambda / (\beta \cos\theta) \quad (2)$$

Thermal gravimetric/ differential thermal analysis

A known amount of the selected samples (SEM; Figs. 2A and B, Fig. 4C, and Fig. 5C) was heated in the TG/DTA balance at the fixed ramp rate ($10^\circ\text{C}/\text{min}$) up to 600°C in the atmosphere of air. The resulted weight loss for the tested particle systems (Figs. 2A and B, Fig. 4C and Fig. 5C) was recorded as a function of temperature (Fig. 11). Thermogravimetric variation for all the samples was the same despite having a difference in the particle morphology. It was observed that the thermal data of the tested material were not affected by the particle's morphology. The parallel DTA curves of the thermally analyzed particle systems are shown in Fig. 12.

The TGA profile (Fig. 11) disclosed nearly 2% weight loss up to 100°C was accredited to the physically adsorbed water molecules and gases, as stated in the literature [18]. Beyond 100°C , two well-defined weight loss steps were observed, which were in agreement with the literature reports [17, 41, 42]. It means that these particles were thermally decomposed into two steps. In the range of 100°C to 275°C , the water of crystallization (2 moles) was removed from the as-prepared dihydrate nickel oxalate with a loss of 20.88% weight producing nickel oxalate (anhydrous) [2]. In addition, a broad endothermic peak was observed at 255°C in the DTA curve (Fig. 12). In comparison, a weight loss of 37.78% in the second step was noted in the range of 275 - 500°C [22, 35]. The observed weight loss was ascribed to the transformation into nickel oxide from anhydrous nickel oxalate. The rate of change in the second step was designated by a sharp prominent exothermic peak as shown in the DTA curve (Fig. 12) [4, 18].

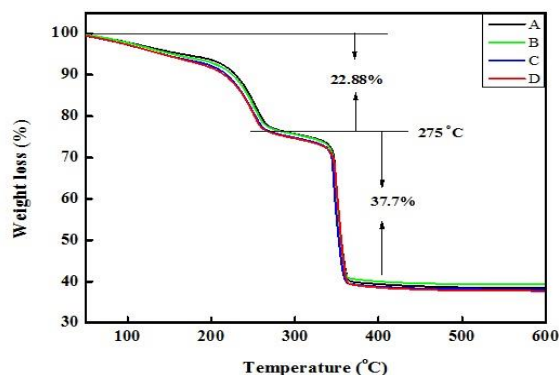


Fig. 11: TGA plots of the as-prepared particles shown in (A) SEM; Fig. 2A, (B) SEM; Fig. 2B, (C) SEM; Fig. 4C, and (D) SEM; Fig. 5C.

Table-2: Crystallite size of the as-prepared uniform particles of different morphologies, calculated from the XRD (Fig. 10).

Sample	2θ (°) (Fig 10)	Intensity (CPS)	FWHM (°)	Crystallite size (nm)
SEM; Fig 2A	18.75	1038	0.3904	40
SEM; Fig 2B	18.75	1415	0.402	39
SEM; Fig 4C	18.75	1223	0.4108	38
SEM; Fig 5C	18.75	749	0.4098	38

Table-3: TGA weight losses and the corresponding calculated activation energies for the uniform NiC₂O₄.2H₂O particles of various morphologies prepared at 25 °C.

Sample	Temperature (°C)	Weight Loss (%)		Ea (kJ/mol)
		Experimental (TGA)	Theoretical (Equation-4)	
Step1	130-250	19.00	19.69	0.099
Step2	250-500	39.03	39.40	1.22

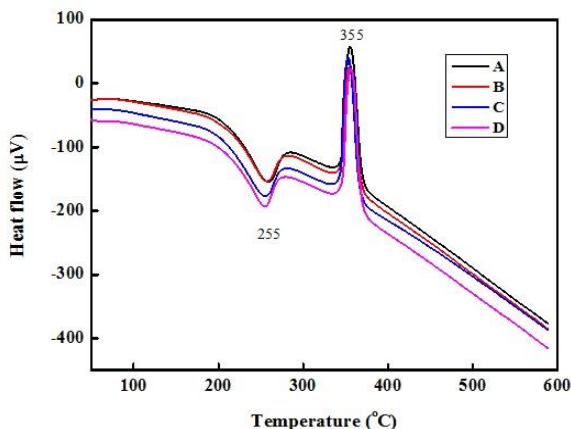
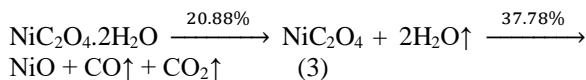


Fig. 12: DTA plots of the particles presented in (A) SEM; Fig. 2A, (B) SEM; Fig. 2B, (C) SEM; Fig. 4C, and (D) SEM; Fig. 5C.

The weight loss steps in the TGA curve were signified by the chemical reaction (3). The total loss in weight investigated experimentally from TGA (58.66%) agreed with that theoretically calculated (59.58%) from the suggested equation (3) [14].



The matching of theoretical and practical weight loss strengthens the suggested equation (Equation-3) for transforming nickel oxalate to nickel oxide. Furthermore, the activation energies related to the thermal variations of the test samples were calculated from the TGA data (typical sample, Fig. 11D) using the Coats-Redfern equation [43] (Equation-4).

$$\ln[-\ln(1-\alpha/T^2)] = E_a/RT + \ln[(AR/\beta E)(1-(2RT/E))] \quad (4)$$

where,

β , the heating rate,
 $\ln[(AR/\beta E)(1-(2RT/E))]$, a constant quantity,
 R, the gas constant equal to 8.314 J/mol/K,
 T, the temperature (absolute),

A, the decomposed material at the time “t”.
 α is the decomposition fraction at time “t”.

The α was calculated from the following Equation (5):

$$\alpha = (W_i - W_t) / (W_i - W_f) \quad (5)$$

The quantity of α was calculated from the particular part of the TGA (Fig 11D) and the resulting data were plotted in Fig. 13. Similarly, for “ $\ln[-\ln(1-\alpha/T^2)]$,” the α values were put in Equation 4, and it was then plotted against 1/T rendering to Eqn. 4 (Fig. 14) for two steps (step 1 and step 2) as shown in Fig. 13. The energies of activation were measured from the slopes (Fig. 14) for these steps and are listed in Table-3. The observed activation energy confirmed the phase transformation through chemical changes during heating. The activation energy observed for step 1 was attributed to the elimination of water of crystallization. In contrast, the high value for step 2 was accredited to the phase change from the as-prepared nickel compound to crystalline NiO particles.

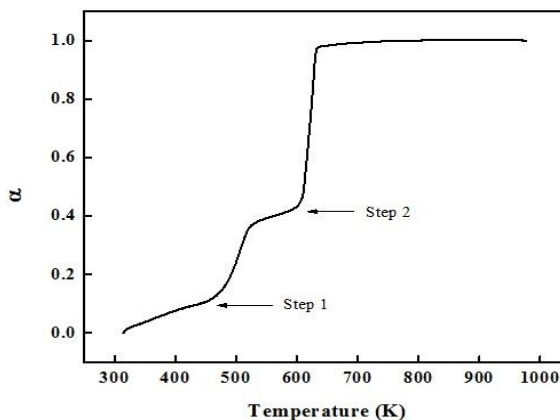


Fig. 13: Change in decomposition fraction (α) against temperature (T) for Fig. 11 D.

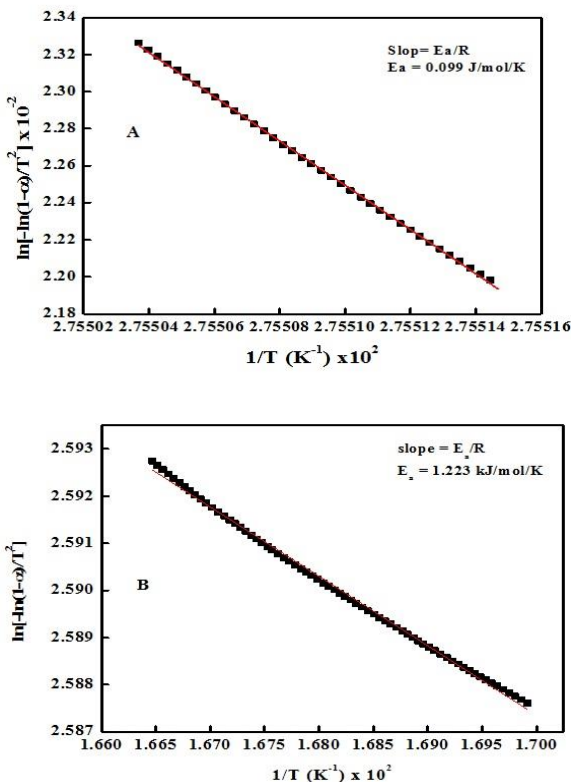


Fig. 14: The plot of $\ln[-\ln(1-\alpha)/T^2]$ vs. $1/T$ for step 1 (A) step 2 (B) as indicated in Fig 13.

Conclusions

- Monodispersed particles of $\text{NiC}_2\text{O}_4 \cdot 2\text{H}_2\text{O}$ in novel morphologies were successfully synthesized from nickel chloride and oxalic acid under an optimized set of reaction conditions.
- The uniform particle systems were precipitated without using any surfactant or shape modifier, as it affected the performance of synthesized powder in its applications. Instead, a green method was adopted under the extensive optimized reaction conditions during the precipitation experiment.
- The optimizations of the experimental parameters strongly affected the synthesized particle's morphology and uniformity.
- Amongst the applied molar ratios of nickel chloride and oxalic acid, the synthesis recipe containing nickel salt concentration 4th times higher than that of the oxalic acid resulted in the formation of the cubic particles of smaller size at 25 °C.
- The cubic shape particles converted to toffee shape with the increase in reaction temperature.

- The particle size also linearly changed with the aging time of the reaction.
- The particle's size and morphology were found to depend on the reagent's molar ratio, but the thermal and spectral profile of test samples were found less affected.
- The crystallinity and crystallite size of the test material increased linearly with increasing the nickel content in the mixture.

Acknowledgments

The authors are highly grateful to the NCEPC, University of Peshawar, KPK, and the Higher Education Commission (HEC) of Pakistan for assisting this research study.

References

1. T. Ahmad, A. Ganguly, J. Ahmed, A. K. Ganguli, O. A. A. Alhartomy, Nanorods of transition metal oxalates: A versatile route to the oxide nanoparticles, *Arab. J. Chem.*, **4**, 125 (2011).
2. F. Behnoudnia, H. Dehghani, Anion effect on the control of morphology for $\text{NiC}_2\text{O}_4 \cdot 2\text{H}_2\text{O}$ nanostructures as precursors for synthesis of $\text{Ni}(\text{OH})_2$ and NiO nanostructures and their application for removing heavy metal ions of cadmium (II) and lead (II), *Dalton Trans.*, **43**, 3471 (2014).
3. A. Hadeel, A. H. A. Hassan, A. J. Baker, Reduced graphene oxide supported palladium nanoparticles as an efficient catalyst for aerobic oxidation of benzyl alcohol, *AIP Conf. Proc.*, **2290**, 030036 (2020).
4. S. Rakshit, S. Chall, S. S. Mati, A. Roychowdhury, S. Moulik, S. C. Bhattacharya, Morphology control of nickel oxalate by soft chemistry and conversion to nickel oxide for application in photocatalysis, *RSC Adv.*, **3**, 6106 (2013).
5. H. Abbas Alshamsi, S. H. Batool, Synthesis, characterization and photocatalysis of $\gamma\text{-Fe}_2\text{O}_3$ nanoparticles for degradation of Cibacron Brilliant Yellow 3G-P, *Asian J. Chem.*, **30**(2), 273 (2018).
6. H. Abbas Alshamsi, M. Abbas. Al Bedairy, S. Hussein Alwan, Visible light assisted photocatalytic degradation of Rhodamine B dye on CdSe-ZnO nanocomposite: Characterization and kinetic studies, *IOP Conf. Series: Earth Environ. Sci.*, **722**, 012005 (2021).
7. T. Okamoto, R. Ichino, M. Okido, Z. Liu, C. Zhang, Effect of ammonia on the crystal morphology of nickel oxalate precipitates and

- their thermal decomposition into metallic nickel, *Mater. Trans.*, **46**, 171 (2005).
- M. A. Al-Bedairy, H. A. H. Alshamsi, Environmentally friendly preparation of zinc oxide, study catalytic performance of photodegradation by sunlight for Rhodamine B Dye, *Eurasian J. Anal. Chem.*, **13(6)**, em72 (2018).
 - H. A. H. Alshamsi, B. S. Hussain, Hydrothermal preparation of silver doping zinc oxide nanoparticles: study, characterization and photocatalytic activity, *Orient. J. Chem.*, **34(4)**, 1898 (2018).
 - J. Zhu, G. Cao, Y. Li, X. Xi, Z. Jin, B. Xu, W. Li, Efficient utilisation of rod-like nickel oxalate in lithium-ion batteries: A case of NiO for the anode and LiNiO₂ for the cathode, *Scr. Mater.* **178**, 51 (2020).
 - N. Li, Q. Li, X. Guo, M. Yuan, H. Pang, Controllable synthesis of oxalate and oxalate-derived nanomaterials for applications in electrochemistry, *Chem. Eng. J.*, **372**, 551 (2019).
 - G. Cheng, J. Xu, C. Dong, W. Yang, T. Kou, Z. Zhang, Anodization driven synthesis of nickel oxalate nanostructures with excellent performance for asymmetric supercapacitor, *J. Mater. Chem. A*, **2**, 17307 (2014).
 - C. Dong, X. Yan, C. Si, H. Gao, W. Ma, G. Cheng, W. Yang, H. Zhong, Z. Zhang, New-Type nickel oxalate nanostructures for ultrahigh sensitive electrochemical biosensing of glucose, *Adv. Mater. Interfaces*, **3**, 1600197 (2016).
 - E. Romero-Tela, M. Mendoza, R. Escudero, Metamagnetism and weak ferromagnetism in nickel (II) oxalate crystals, *J. Phys. Condens. Matter*, **24**, 196003 (2012).
 - D. Zhang, J. Zhang, H. Wang, C. Cui, W. Jiao, J. Gao, Y. Liu, Novel Ni foam based nickel oxalate derived porous NiO nanostructures as highly efficient electrodes for the electrooxidation of methanol/ethanol and urea, *J. Alloys Compd.*, **806**, 1419 (2019).
 - T. Kou, M. Chen, F. Wu, T. J. Smart, S. W. Wang, Y. S. Wu, Y. Zhang, S. T. Li, S. Lall, Z. H. Zhang, Carbon doping switching on the hydrogen adsorption activity of NiO for hydrogen evolution reaction, *Nat. Commun.*, **11**, 590 (2020).
 - B. Sengupta, C. A. Tamboli, R. Sengupta, Synthesis of nickel oxalate particles in the confined internal droplets of W/O emulsions and in systems without space confinement, *Chem. Eng. J.*, **169**, 379 (2011).
 - T. Li, Y. Liu, T. Peng, G. Ma, X. Yang, Controlled synthesis of polycrystalline nickel oxalate nanofibers by the mild thermal precipitation and aging process, *J. Wuhan Univ. Technol. Mater. Sci. Ed.*, **26**, 1041 (2011).
 - H. Oudghiri-Hassani, F. Al Wadaani, Preparation, Characterization and Catalytic Activity of Nickel Molybdate (NiMoO₄) Nanoparticles, *Molecules*, **23**, 273 (2018).
 - I. Jung, Y. Lee, Y. Tak, J. Choi, Nickel Oxalate Nanowires Grown on Electrochemically Deposited Ni Thin Film, *J. Electrochem. Soc.*, **158**, D123 (2011).
 - J. Zhao, Y. Tian, A. Liu, L. Song, Z. Zhao, The NiO electrode materials in electrochemical capacitor: A review, *Mat. Sci. Semicon. Proc.*, **96**, 78 (2019).
 - I. U. Haq, F. Haider, Synthesis and characterization of uniform fine particles of nickel compounds, *J. Chin. Chem. Soc.*, **57**, 343 (2010).
 - Z. Qi, Y. Wu, X. Li, Y. Qu, Y. Yang, D. Mei, Microwave-assisted synthesis of CuC₂O₄·xH₂O for anode materials in lithium-ion batteries with a high capacity, *Ionics*, **26**, 33-42 (2020).
 - K. Zhang, R. Xu, R. Wei, Y. Li, Y. Wang, Y. Zhang, Y. Dai, Y. Yao, Tunable polymorph and morphology synthesis of iron oxalate nanoparticles as anode materials for Lithium ion batteries, *Mater. Chem. Phys.*, **243**, 122676 (2020).
 - Z. Liu, H. Ma, Z. Liu, Synthesis of fibrous cobalt oxalate by a double-jet process: morphology and growth control, *JOM*, **71**, 2884 (2019).
 - X. Chen, X. Liu, K. Huang, Facile synthesis of flake-like dihydrate zinc oxalate particles, *Int. J. Miner. Metall. Mater.*, **26**, 234 (2019).
 - Z. Lin, S. Liu, J. -G. Li, J. Chen, M. Xie, X. Li, M. Zhang, Q. Zhu, D. Huo, X. Sun, Morphology-controllable synthesis and thermal decomposition of Ag and Ni oxalate for Ag-Ni alloy electrical contact materials, *Mater. Des.*, **108**, 640 (2016).
 - X. Wang, J. Song, L. Gao, J. Jin, H. Zheng, Z. Zhang, Optical and electrochemical properties of nanosized nio via thermal decomposition of nickel oxalate nanofibres, *Nanotechnology*, **16**, 37 (2005).
 - T. Ahmad, K. V. Ramanujachary, S. E. Lofland, A. K. Ganguli, Magnetic and electrochemical properties of nickel oxide nanoparticles obtained by the reverse-micellar route, *Solid State Sci.*, **8**, 425 (2006).
 - S. Vaidya, P. Rastogi, S. Agarwal, S. K. Gupta, T. Ahmad, Jr. A. M. Antonelli, K. Ramanujachary, S. Lofland, A. K. Ganguli, Nanospheres, nanocubes, and nanorods of nickel oxalate: control of shape and size by surfactant

- and solvent, *J. Phys. Chem. C*, **112**, 12610 (2008).
31. Y. -Q. Fan, C. -F. Zhang, J. -H. Wu, Z. Jing, Y. Ping, Composition and morphology of complicated copper oxalate powder, *Trans. Nonferrous Met. Soc. China*, **20**, 165 (2010).
 32. L. Zhaogang, L. Mei, H. Yanhong, W. Mitang, S. Zhenxue, Preparation of large particle rare earth oxides by precipitation with oxalic acid, *J. Rare Earths*, **26**, 158 (2008).
 33. A. Wang, H. Yin, H. Lu, J. Xue, M. Ren, T. Jiang, Catalytic activity of nickel nanoparticles in hydrogenation of p-nitrophenol to p-aminophenol, *Catal. Commun.*, **10**, 2060 (2009).
 34. T. Okamoto, J. G. Yang, K. Kuroda, R. Ichino, M. Okido, In Preparation of size and aggregation controlled nickel oxalate dihydrate particles from nickel hydroxide, *Adv. Mater. Res.* **15-17**, 581 (2007).
 35. Z. Jia, J. Liu, Q. Wang, M. Ye, R. Zhu, Facile preparation of mesoporous nickel oxide microspheres and their adsorption property for methyl orange from aqueous solution, *Mat. Sci. Semicon. Proc.*, **26**, 716 (2014).
 36. T. Ahmad, R. Chopra, K. V. Ramanujachary, S. E. Lofland, A. K. Ganguli, Nanorods of copper and nickel oxalates synthesized by the reverse micellar route, *J. Nanosci. Nanotechnol.*, **5**, 1840 (2005).
 37. M. C. López, J. Tirado, C. P. Vicente, Structural and comparative electrochemical study of M (II) oxalates, M= Mn, Fe, Co, Ni, Cu, Zn, *J. Power Sources*, **227**, 65 (2013).
 38. B. Małecka, A. Małecki, E. Drożdż-Cieśla, L. Tortet, P. Llewellyn, F. Rouquerol, Some aspects of thermal decomposition of $\text{NiC}_2\text{O}_4 \cdot 2\text{H}_2\text{O}$, *Thermochim. Acta*, **466**, 57 (2007).
 39. H. -J. Oh, C. -H. Jo, C. S. Yoon, H. Yashiro, S. -J. Kim, S. Passerini, Y. -K. Sun, S. -T. Myung, Nickel oxalate dihydrate nanorods attached to reduced graphene oxide sheets as a high-capacity anode for rechargeable lithium batteries, *NPG Asia Mater.*, **8**, e270 (2016).
 40. A. Monshi, M. R. Foroughi, M. R. Monshi, Modified Scherrer equation to estimate more accurately nano-crystallite size using XRD, *WJNSE*, **2**, 154 (2012).
 41. S. V. Ganachari, R. Bhat, R. Deshpande, A. Venkataraman, Synthesis and characterization of nickel oxide nanoparticles by self-propagating low temperature combustion method, *Recent Res. Sci. Technol*, **4**, 50 (2012).
 42. S. T. Fardood, A. Ramazani, S. Moradi, A novel green synthesis of nickel oxide nanoparticles using Arabic Gum, *Chem. J. Mold*, **12**, 115 (2017).
 43. B. B. Uzun, E. Yaman, Pyrolysis kinetics of walnut shell and waste polyolefins using thermogravimetric analysis, *J. Energy Inst.*, **90**, 825 (2017).